Supporting Material

Manipulating the conformation of 3,2':6',3''-terpyridine in $[Cu_2(\mu\text{-}OAc)_4(3,2':6',3''\text{-}tpy)]_n$ 1D-polymers

Dalila Rocco, Samantha Novak, Alessandro Prescimone, Edwin C. Constable and Catherine E. Housecroft*

Department of Chemistry, University of Basel, BPR 1096, Mattenstrasse 24a, CH-4058 Basel, Switzerland

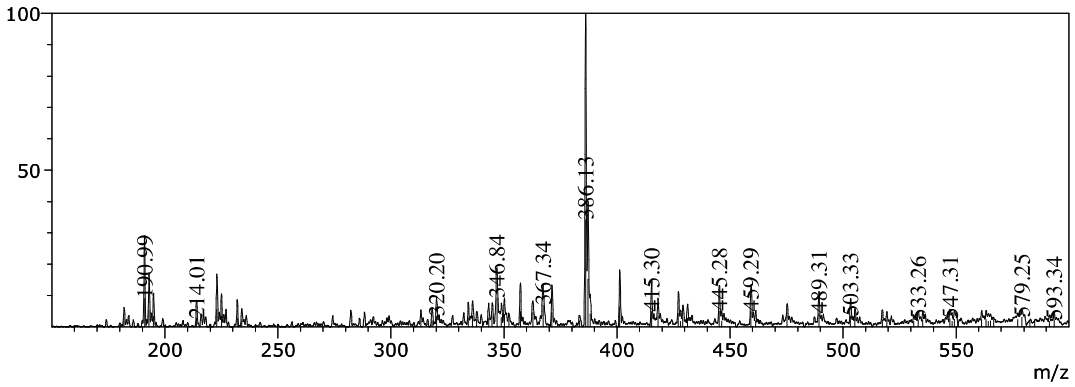

Figure S1. Electrospray mass spectrum of **1**.

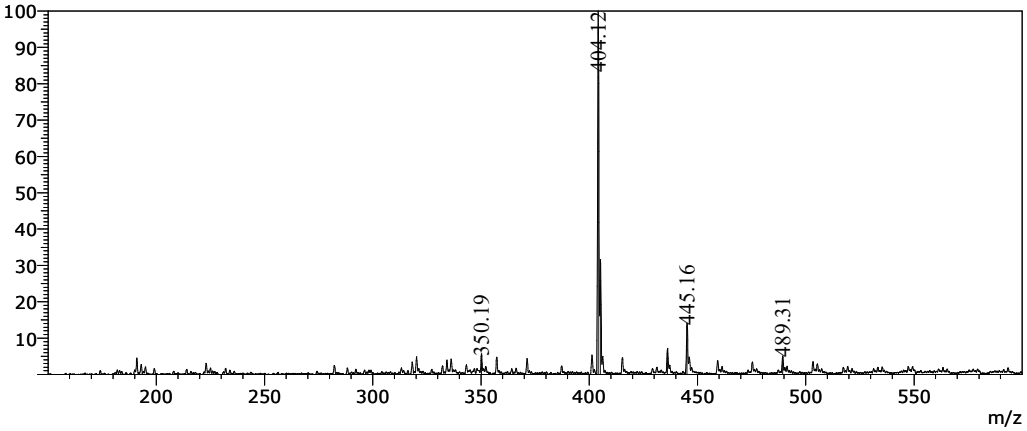

Figure S2. Electrospray mass spectrum of **2**.

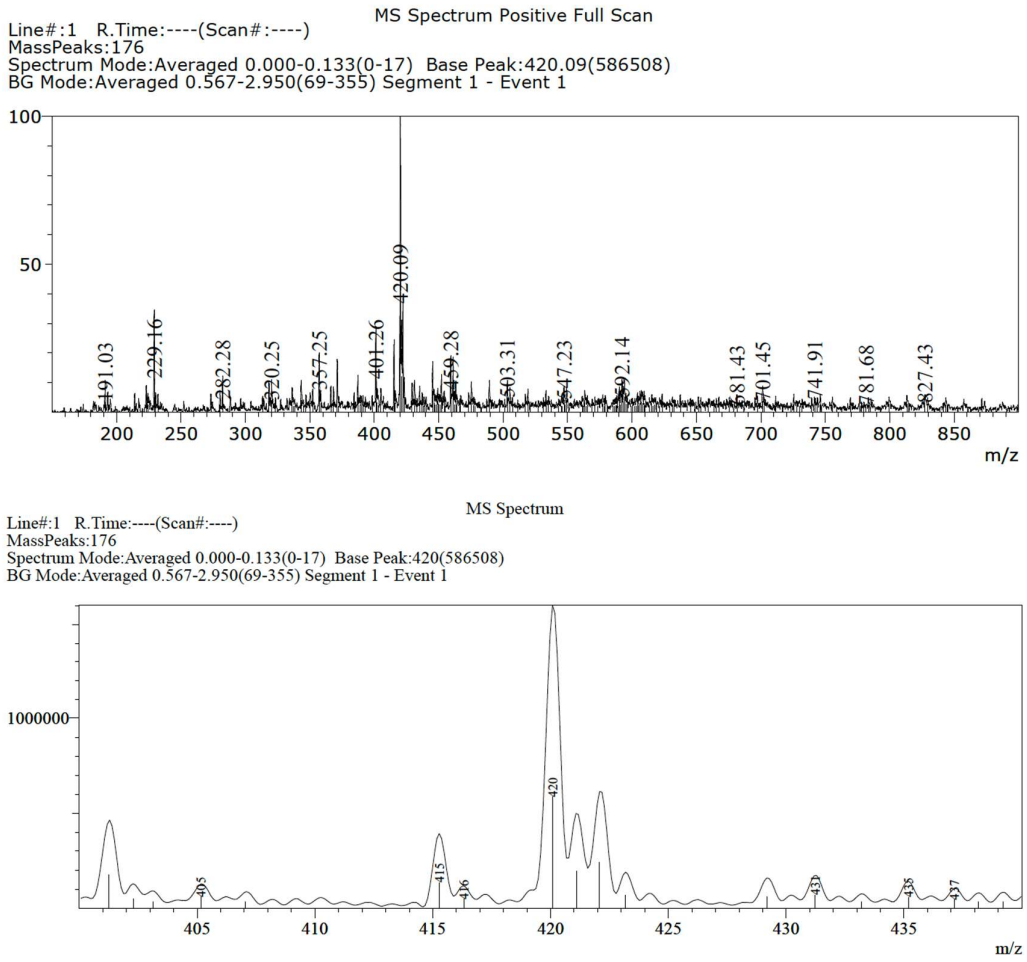

Figure S3. Electrospray mass spectrum of **3**.

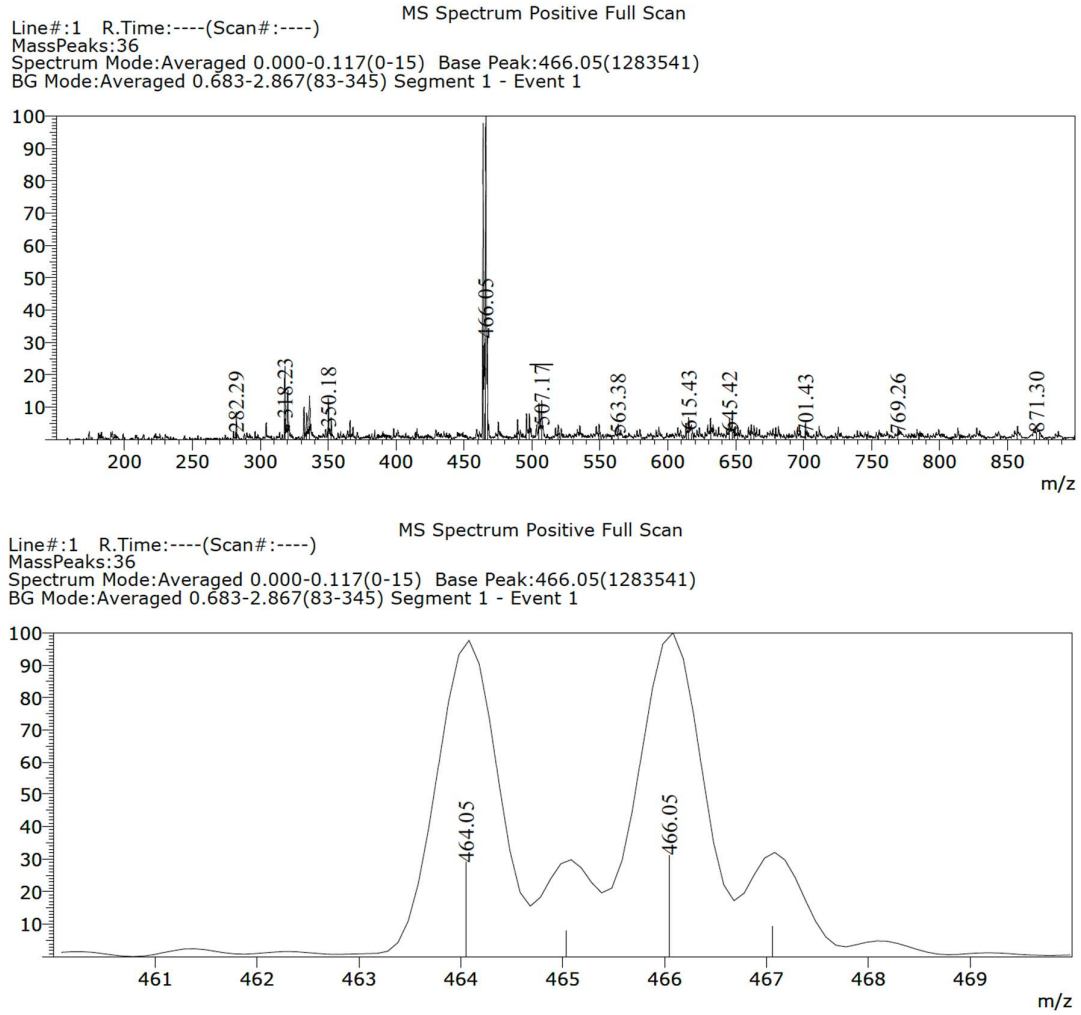

Figure S4. Electrospray mass spectrum of **4**.

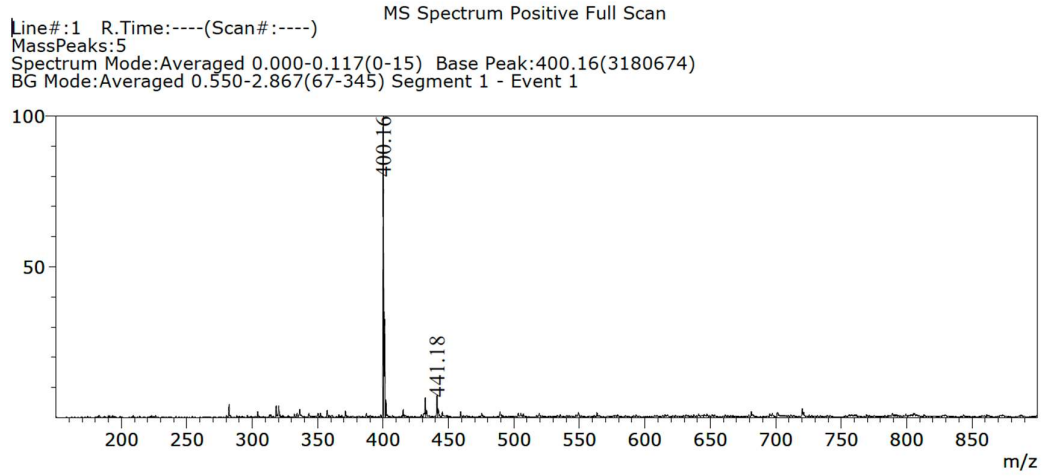

Figure S5. Electrospray mass spectrum of **5**.

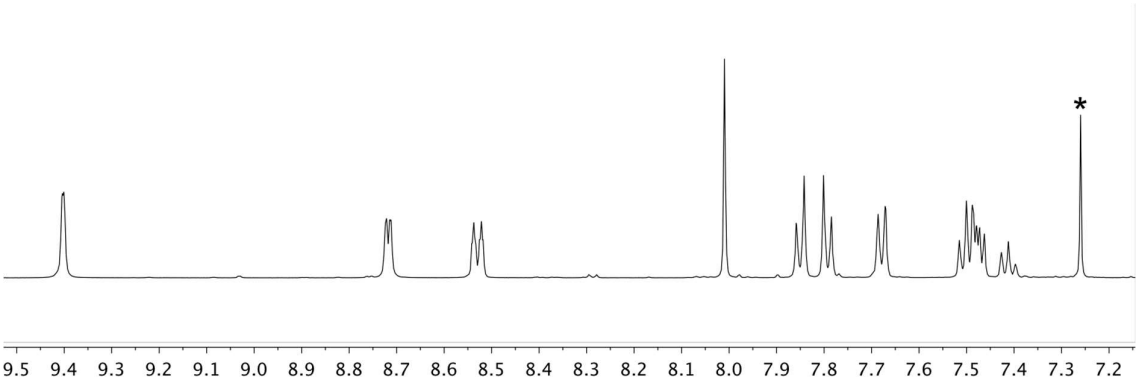

Figure S6. ^{1}H NMR spectrum of **1** (500 MHz, $CDCl_3$, 298 K). * = residual $CHCl_3$.

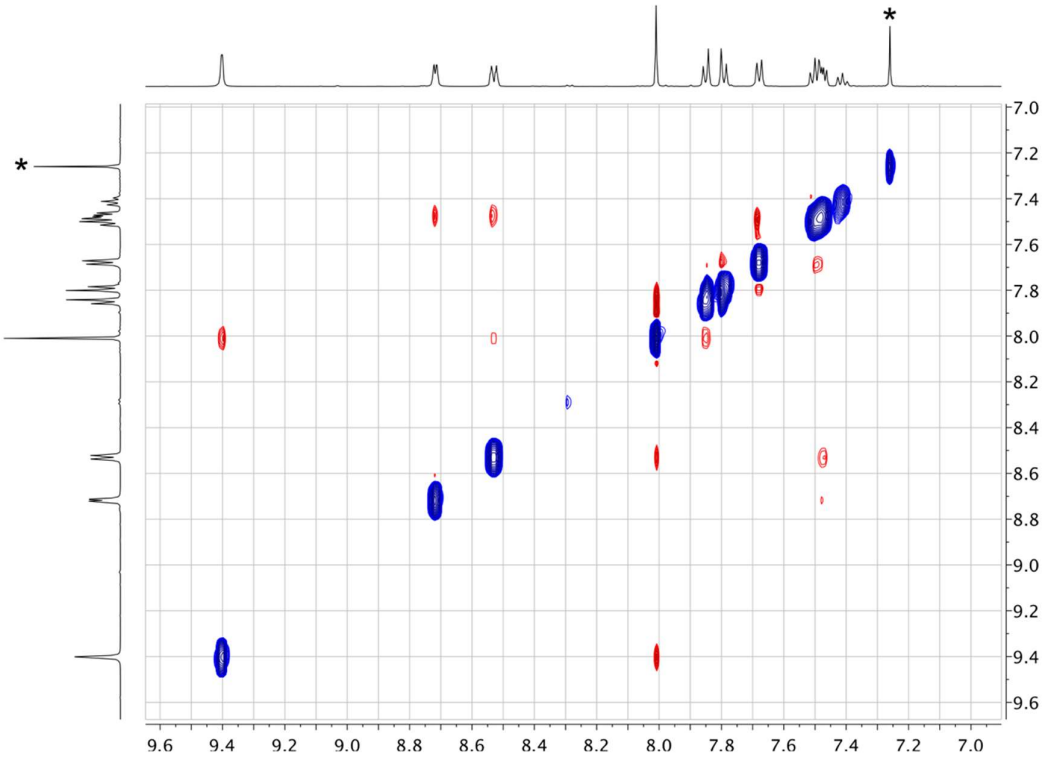

Figure S7. NOESY spectrum of **1** (500 MHz, $CDCl_3$, 298 K). * = residual $CHCl_3$.

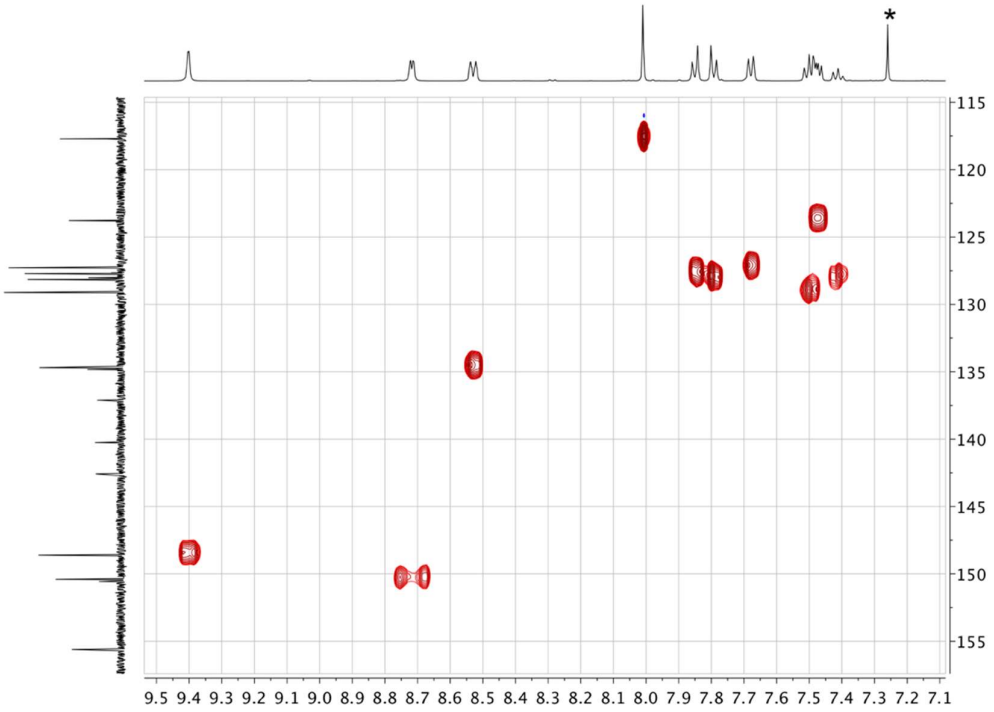

Figure S8. HMQC spectrum of **1** (^{1}H 500 MHz, ^{13}C{^{1}H} 126 MHz, $CDCl_3$, 298 K). * = residual $CHCl_3$.

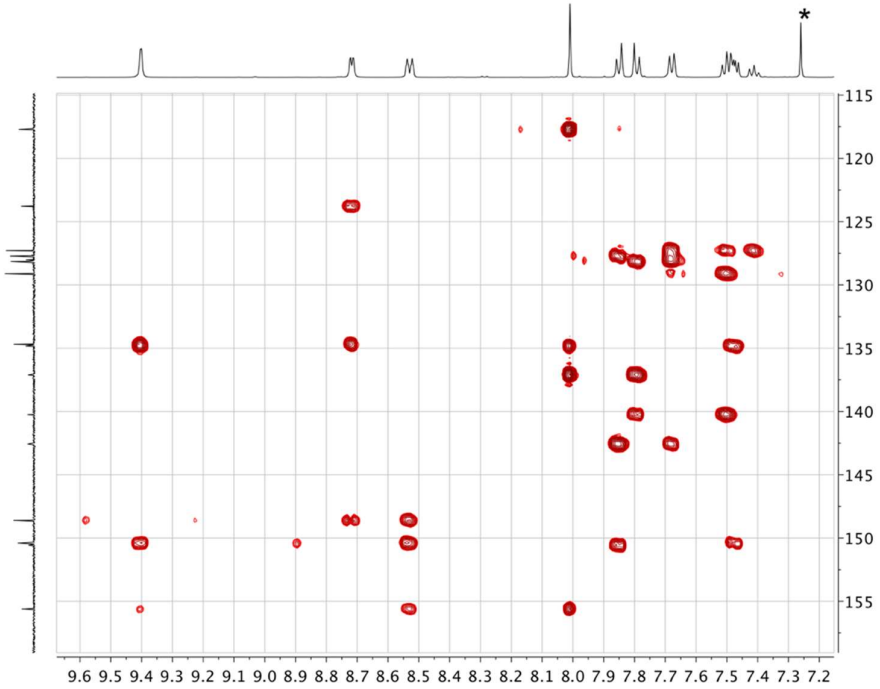

Figure S9. HMBC spectrum of **1** (^{1}H 500 MHz, ^{13}C{^{1}H} 126 MHz, $CDCl_3$, 298 K). * = residual $CHCl_3$.

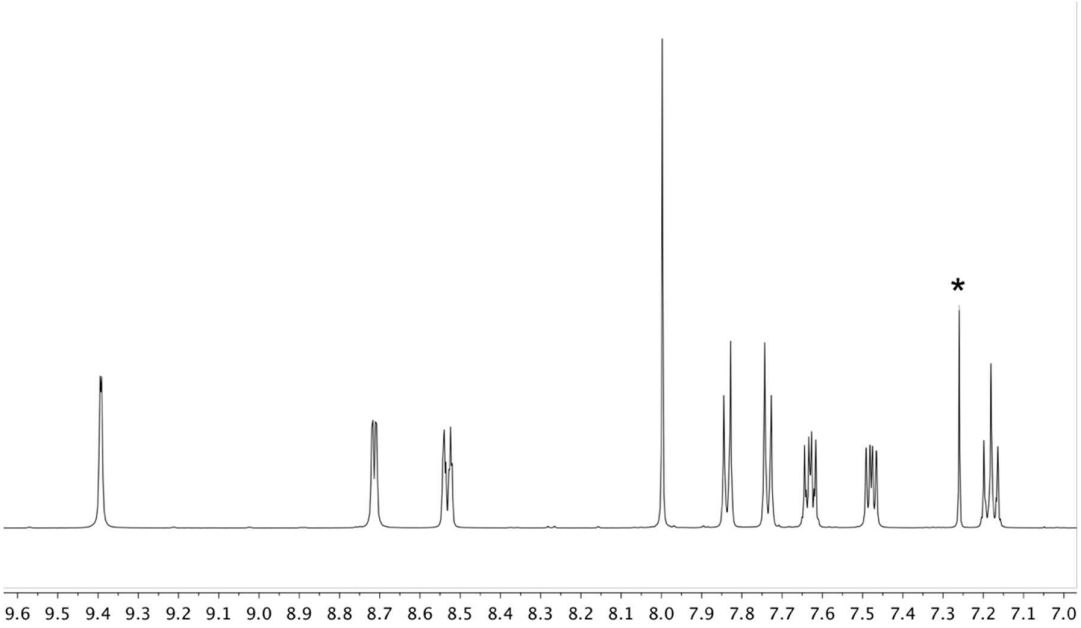

Figure S10. ^{1}H NMR spectrum of **2** (500 MHz, $CDCl_3$, 298 K). * = residual $CHCl_3$.

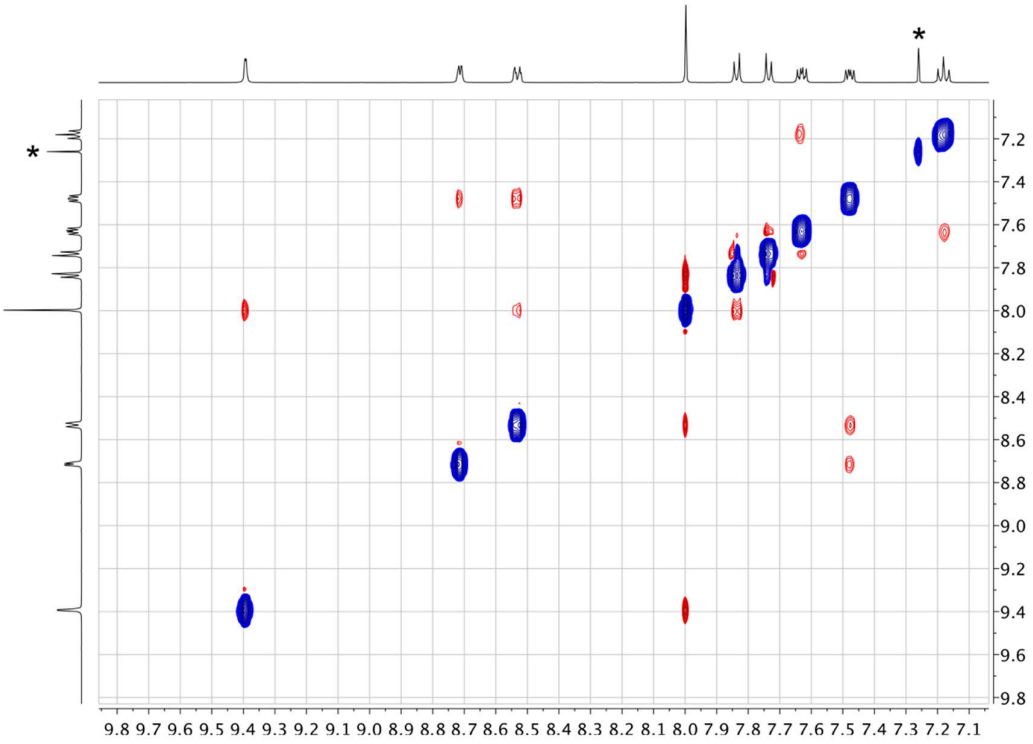

Figure S11. NOESY spectrum of **2** (500 MHz, $CDCl_3$, 298 K). * = residual $CHCl_3$.

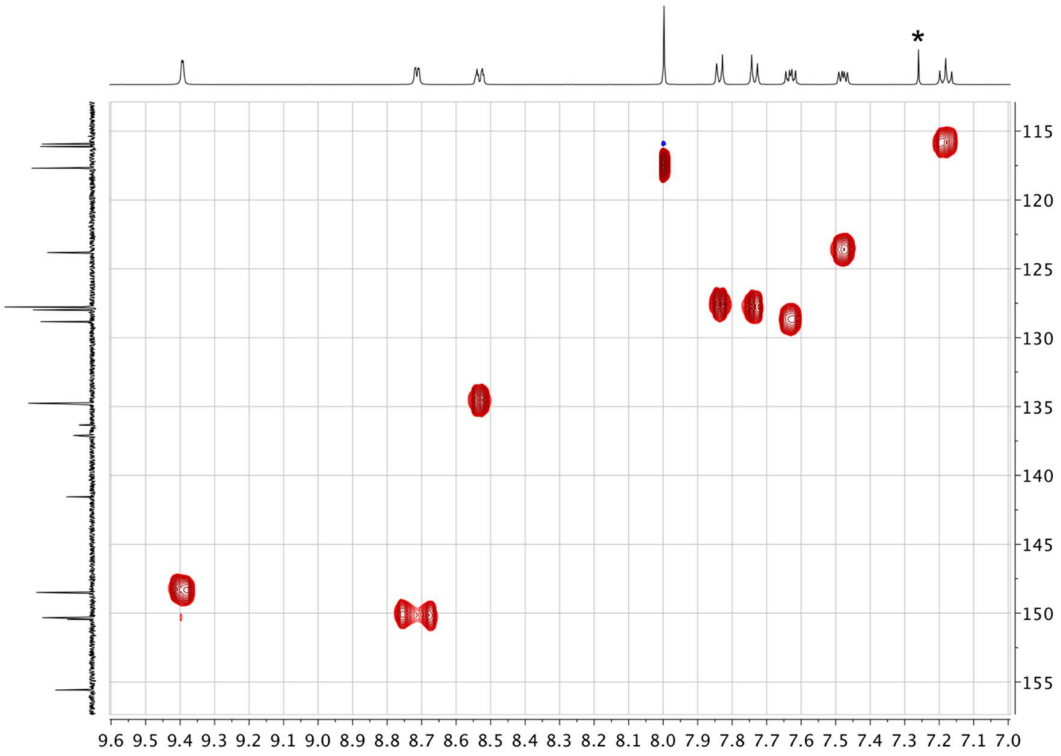

Figure S12. HMQC spectrum of **2** (^{1}H 500 MHz, ^{13}C{^{1}H} 126 MHz, $CDCl_3$, 298 K). * = residual $CHCl_3$.

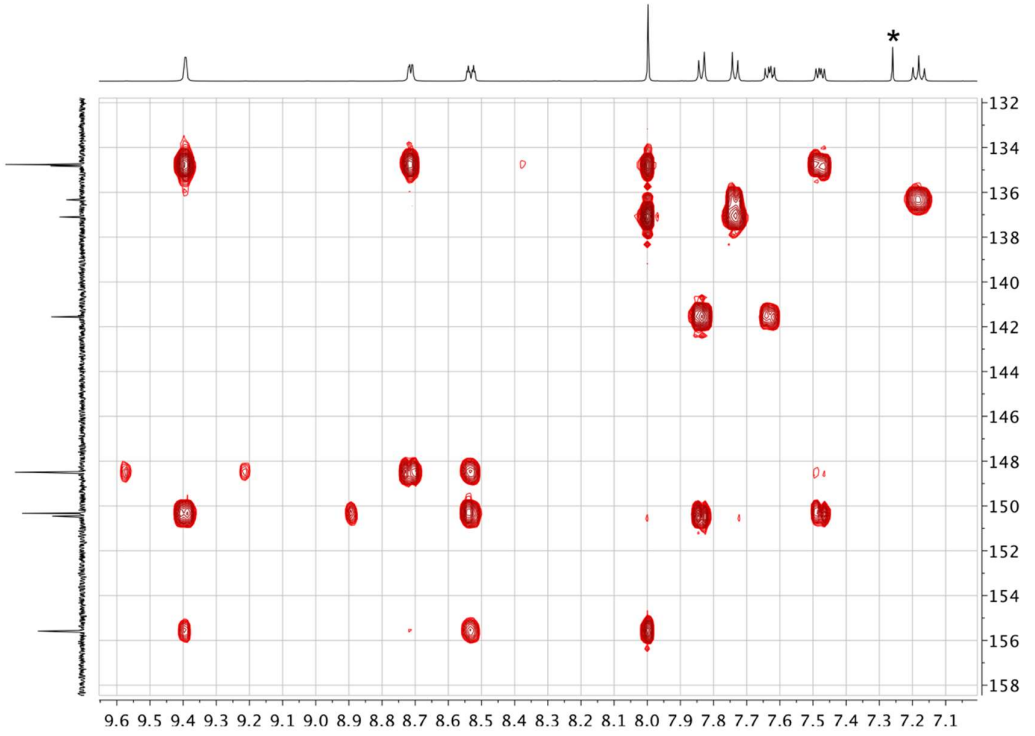

Figure S13. HMBC spectrum of **2** (^{1}H 500 MHz, ^{13}C{^{1}H} 126 MHz, $CDCl_3$, 298 K). * = residual $CHCl_3$.

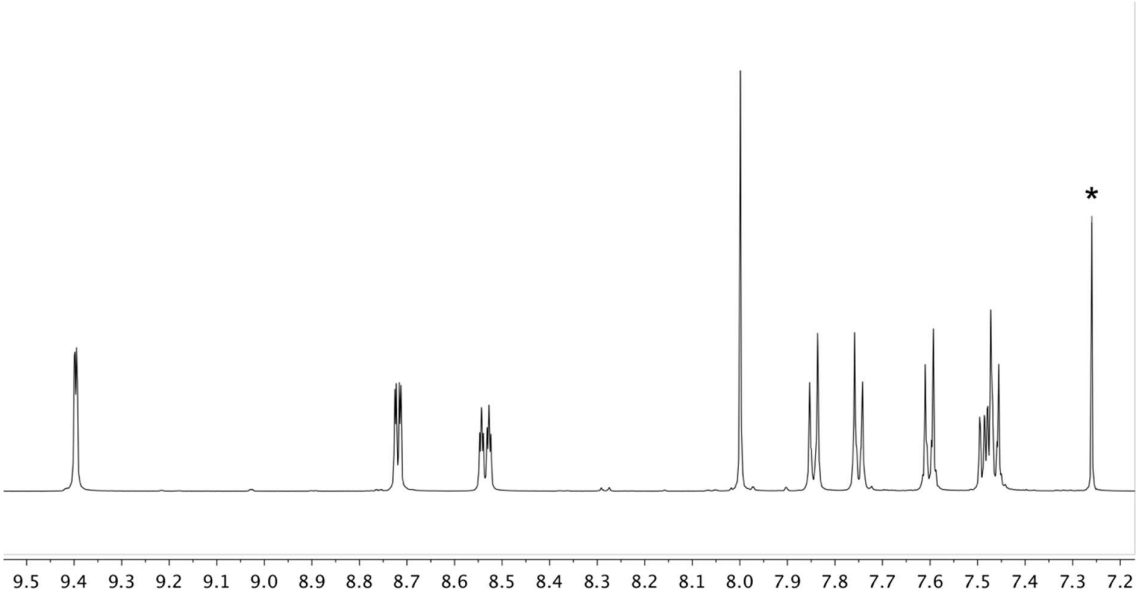

Figure S14. ^{1}H NMR spectrum of **3** (500 MHz, $CDCl_3$, 298 K). * = residual $CHCl_3$.

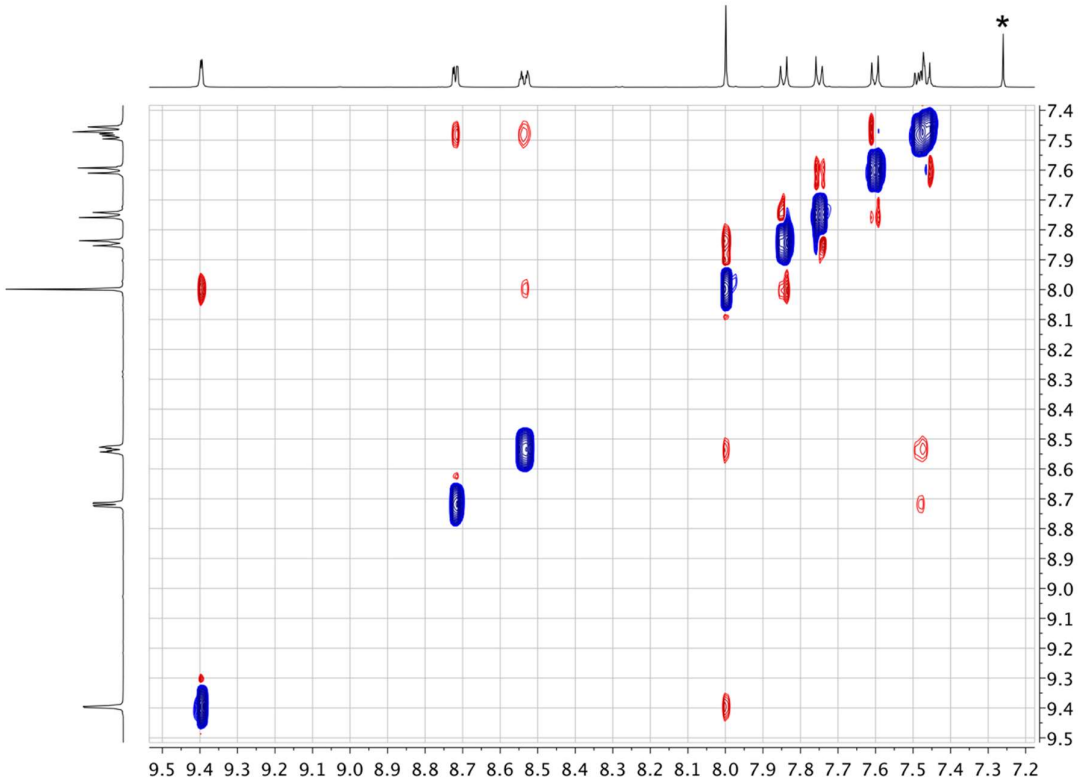

Figure S15. NOESY spectrum of **3** (500 MHz, $CDCl_3$, 298 K). * = residual $CHCl_3$.

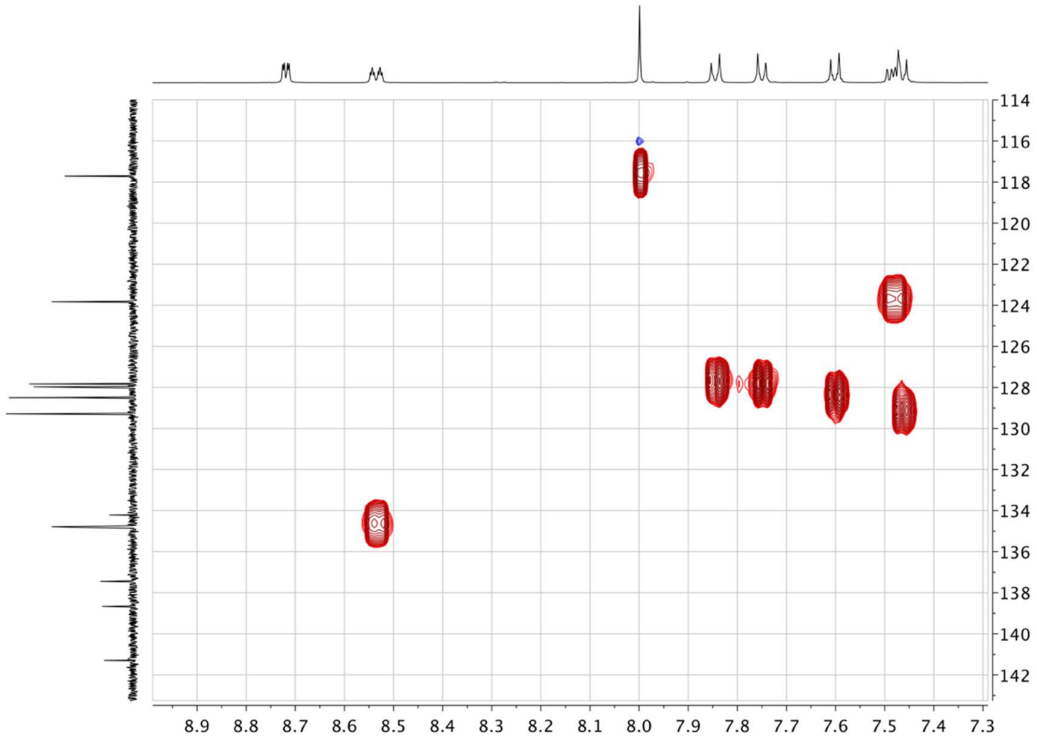

Figure S16. HMQC spectrum of **3** (^{1}H 500 MHz, ^{13}C{^{1}H} 126 MHz, $CDCl_3$, 298 K). * = residual $CHCl_3$.

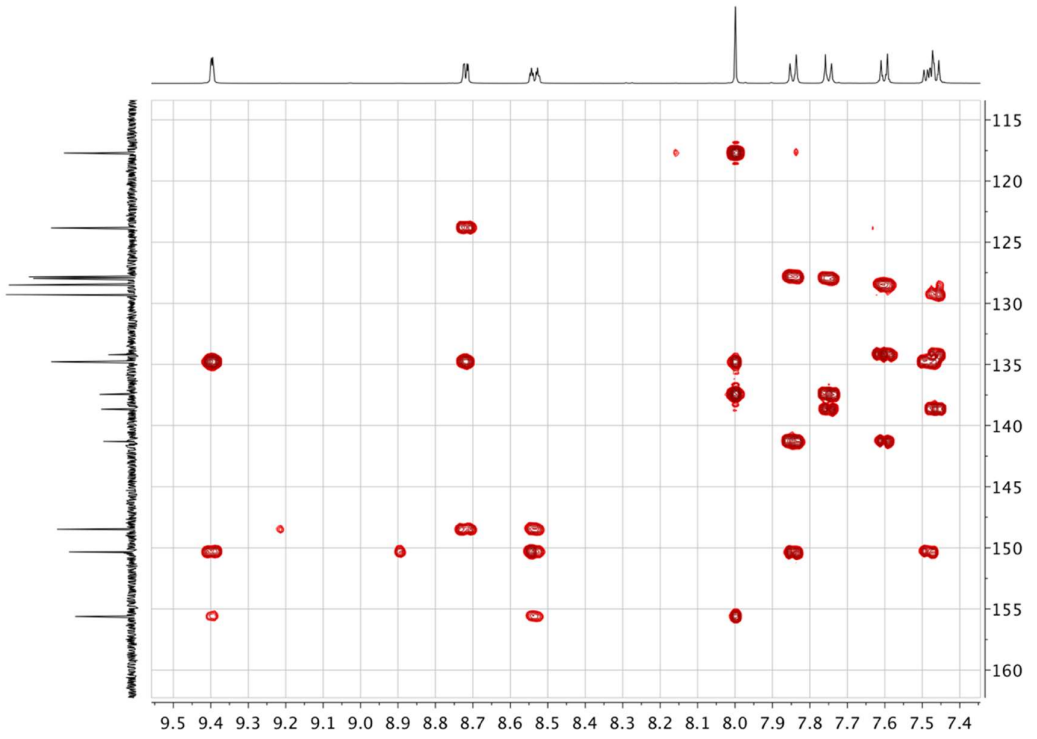

Figure S17. HMBC spectrum of **3** (^{1}H 500 MHz, ^{13}C{^{1}H} 126 MHz, $CDCl_3$, 298 K). * = residual $CHCl_3$.

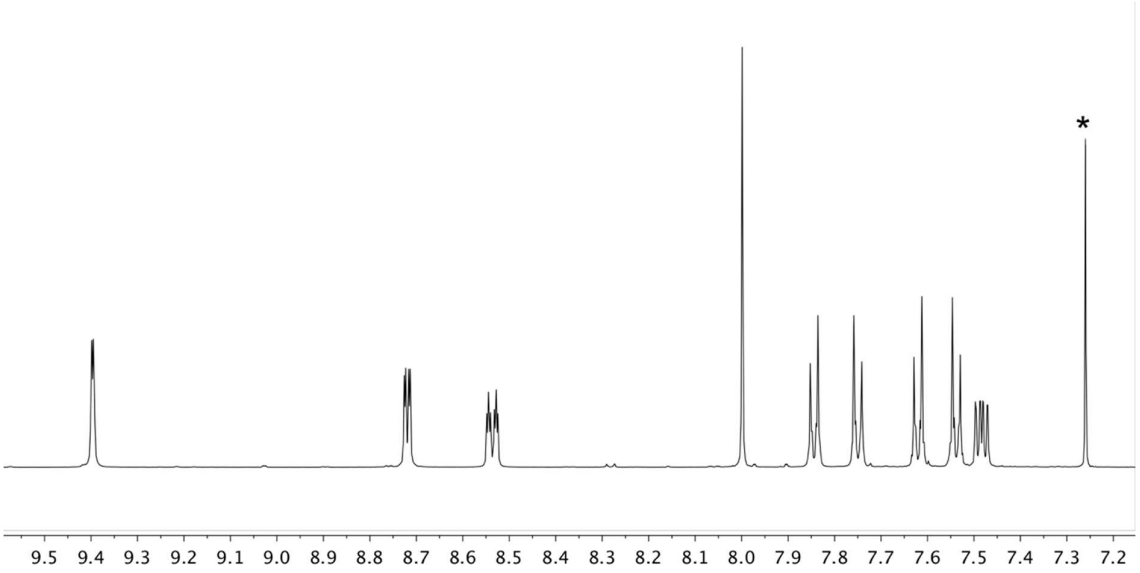

Figure S18. ^{1}H NMR spectrum of **4** (500 MHz, $CDCl_3$, 298 K). * = residual $CHCl_3$.

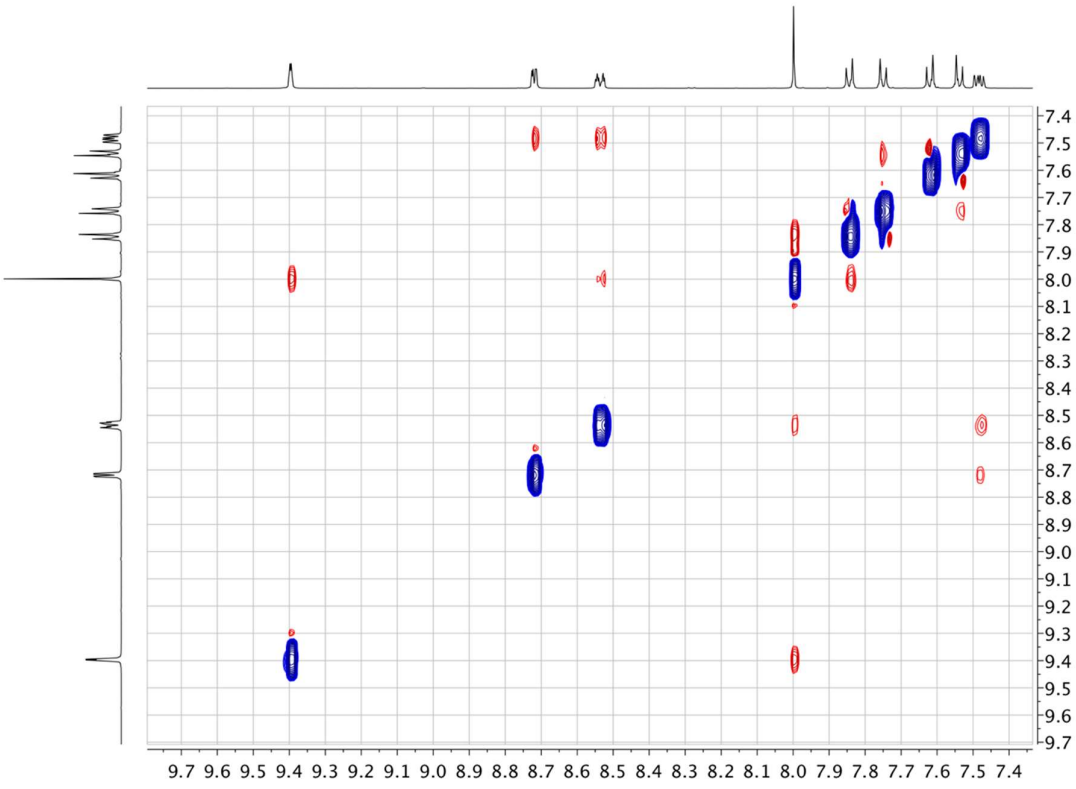

Figure S19. NOESY spectrum of **4** (500 MHz, $CDCl_3$, 298 K). * = residual $CHCl_3$.

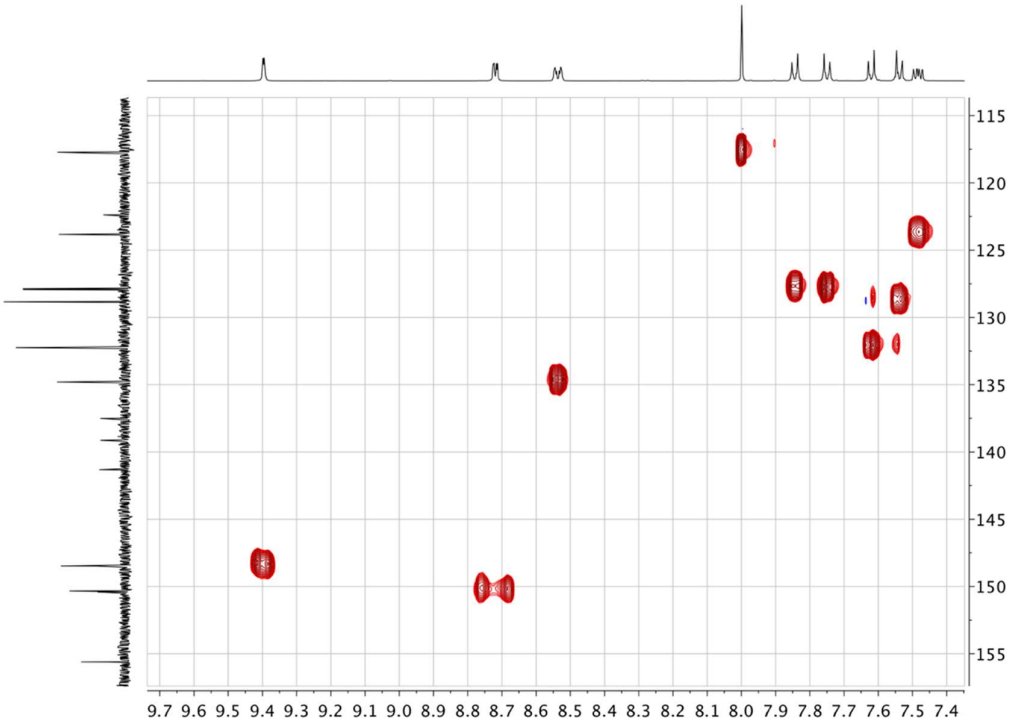

Figure S20. HMQC spectrum of **4** (^{1}H 500 MHz, ^{13}C{^{1}H} 126 MHz, $CDCl_3$, 298 K). * = residual $CHCl_3$.

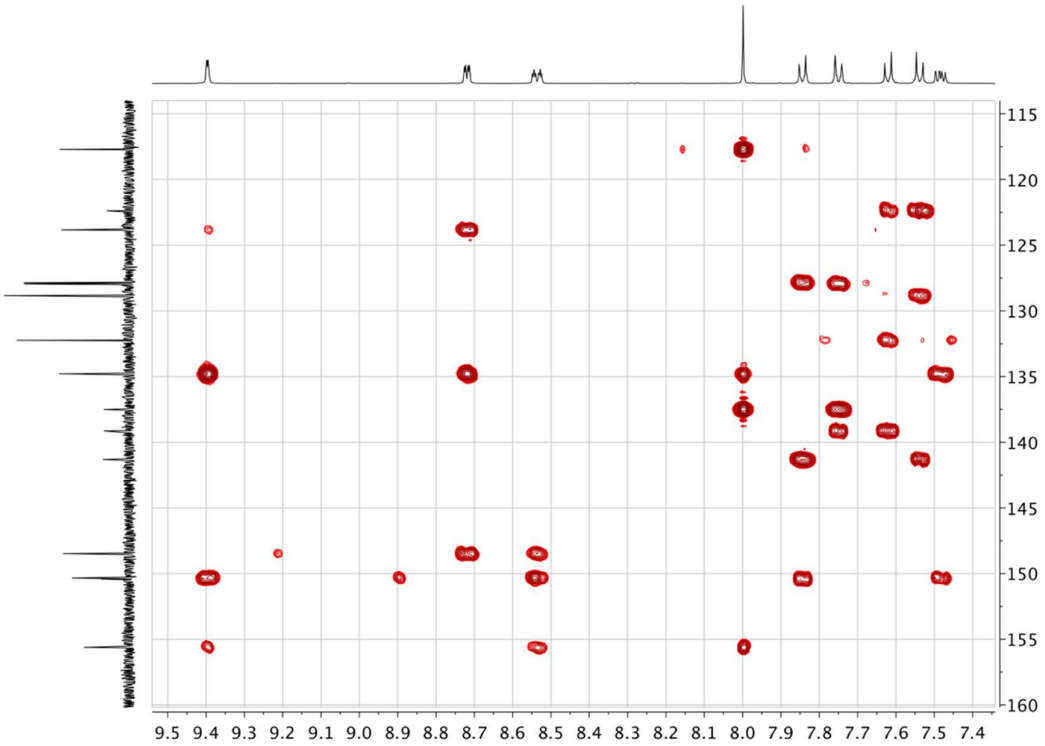

Figure S21. HMBC spectrum of **4** (^{1}H 500 MHz, ^{13}C{^{1}H} 126 MHz, $CDCl_3$, 298 K). * = residual $CHCl_3$.

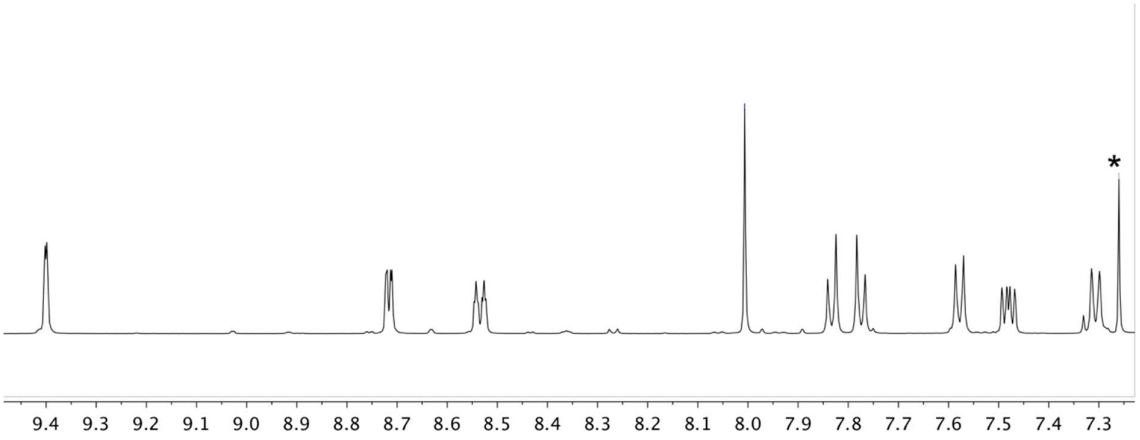

Figure S22. ^{1}H NMR spectrum (aromatic region) of **5** (500 MHz, $CDCl_3$, 298 K). * = residual $CHCl_3$.

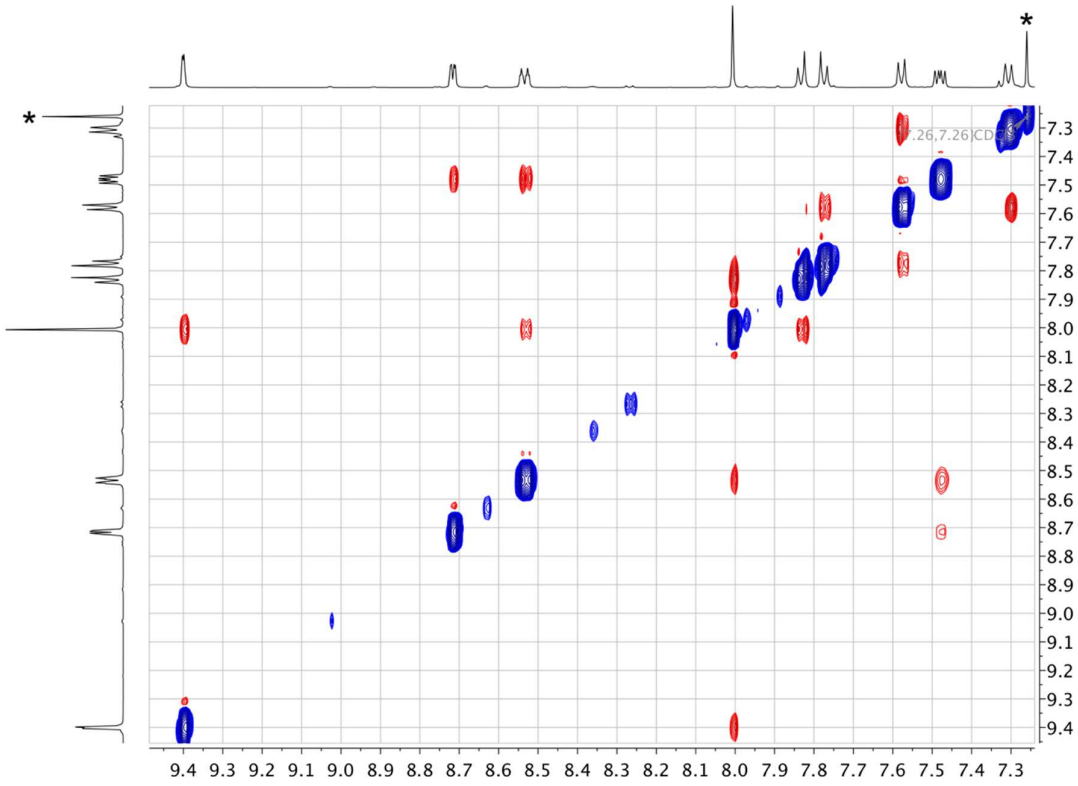

Figure S23. NOESY spectrum (aromatic region) of **5** (500 MHz, $CDCl_3$, 298 K). * = residual $CHCl_3$.

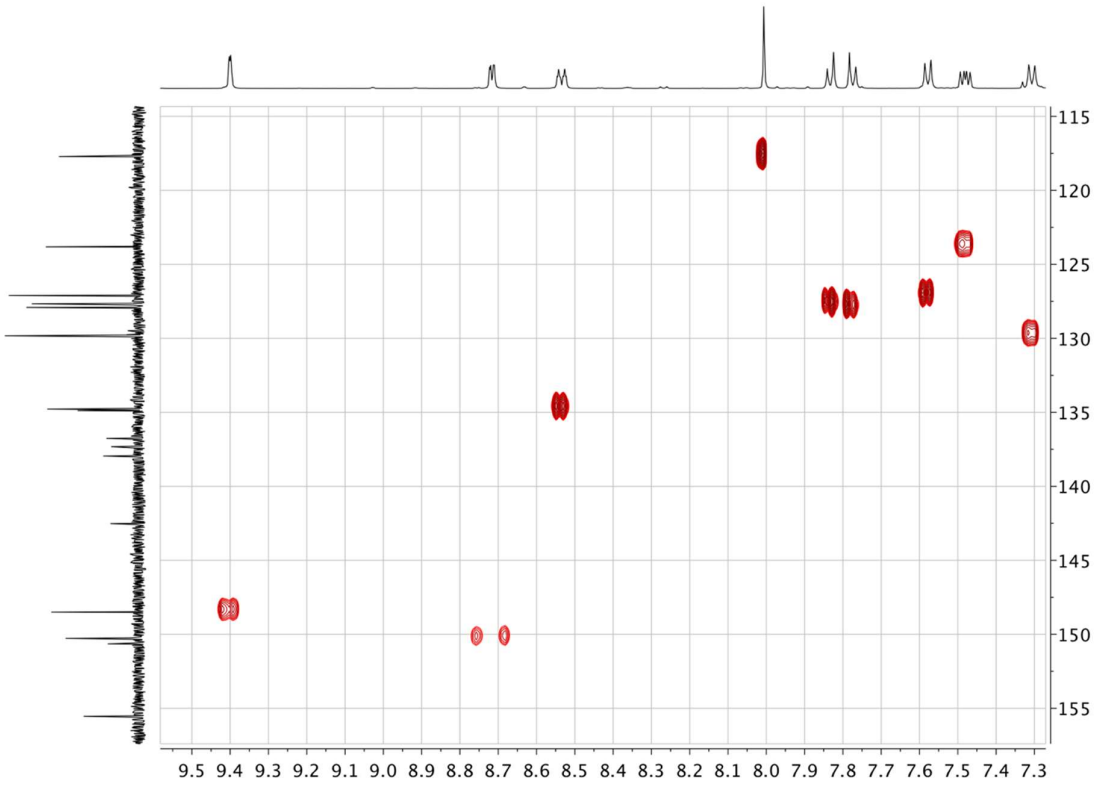

Figure S24. HMQC spectrum (aromatic region) of **5** (^{1}H 500 MHz, ^{13}C{^{1}H} 126 MHz, $CDCl_3$, 298 K). * = residual $CHCl_3$.

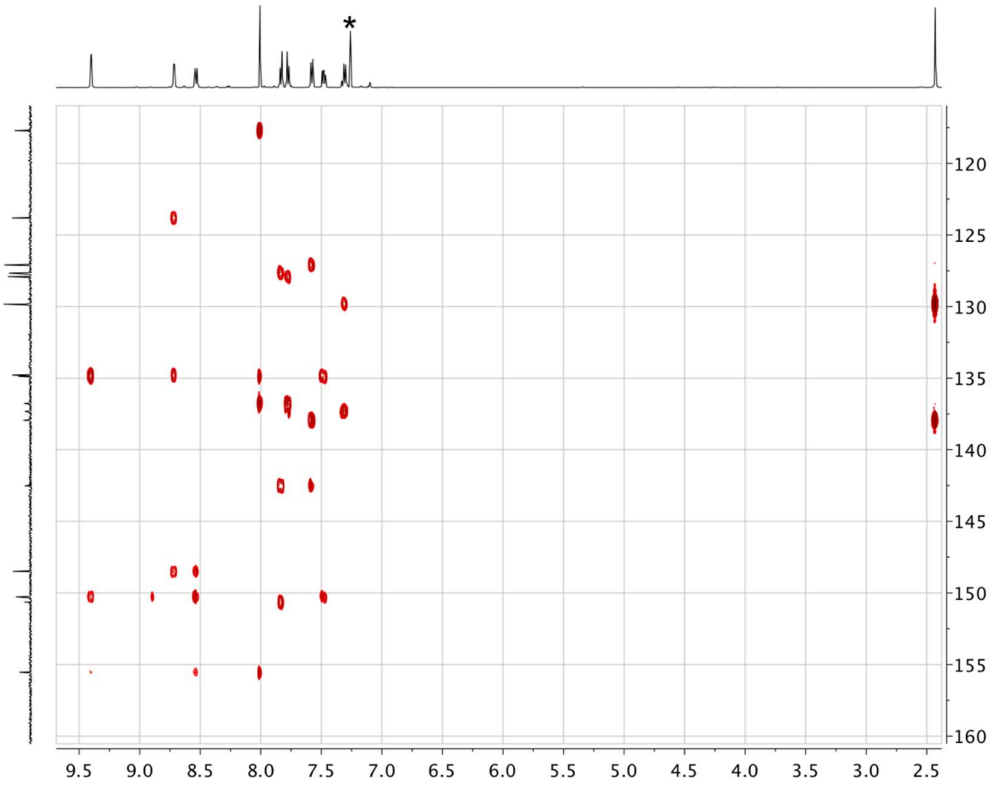

Figure S25. HMBC spectrum of **5** (^{1}H 500 MHz, ^{13}C{^{1}H} 126 MHz, $CDCl_3$, 298 K). * = residual $CHCl_3$.

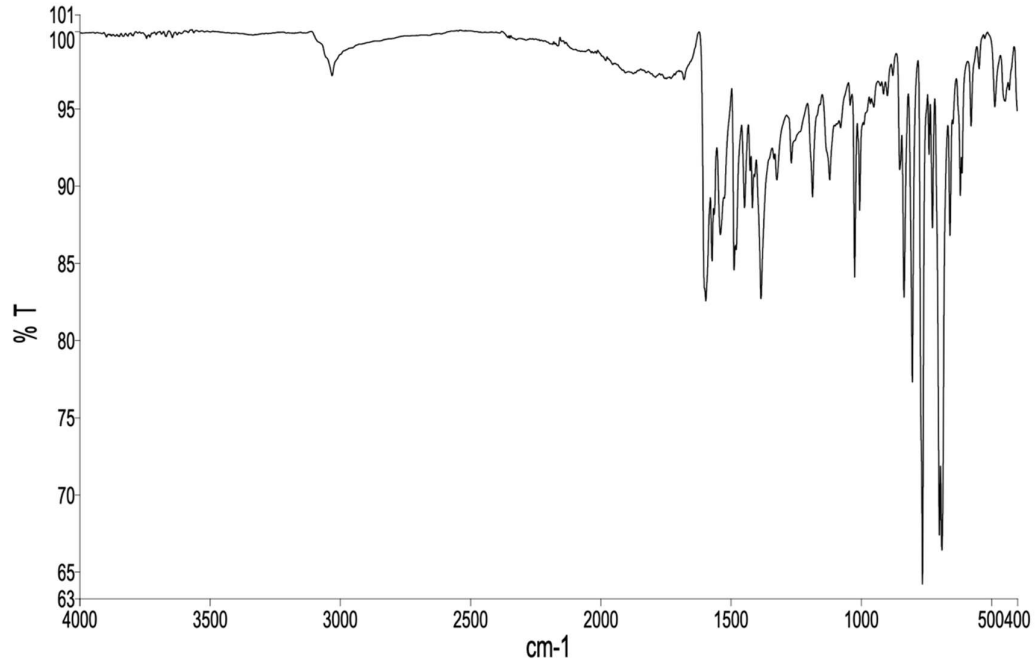

Figure S26. FT-IR spectrum of solid **1**.

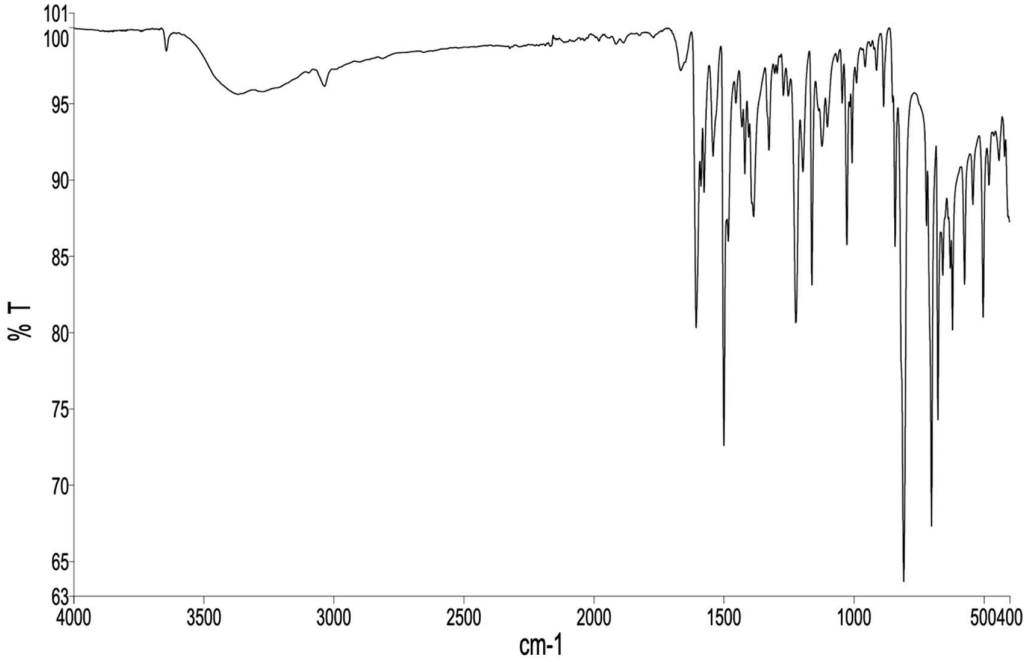

Figure S27. FT-IR spectrum of solid **2**.

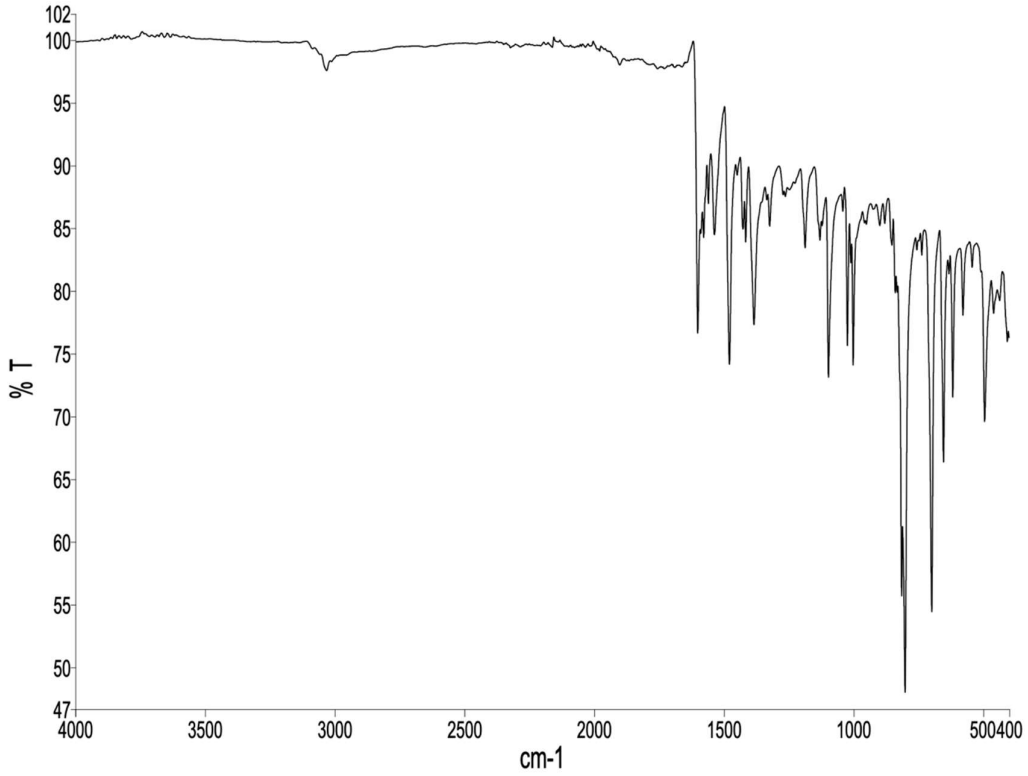

Figure S28. FT-IR spectrum of solid **3**.

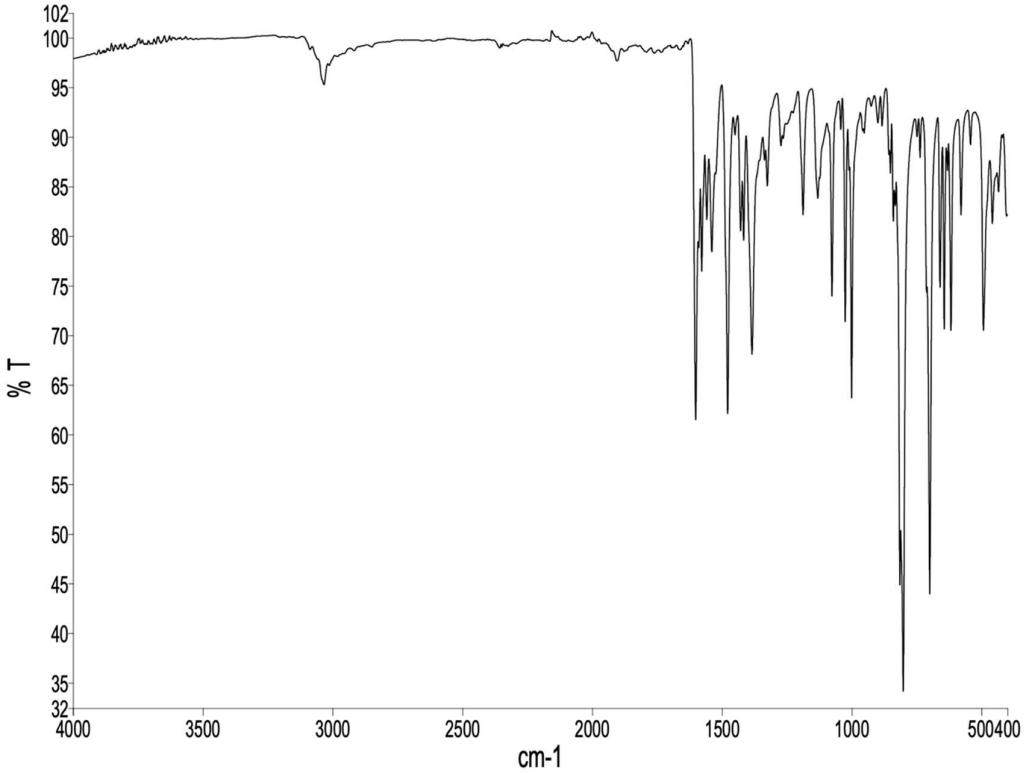

Figure S29. FT-IR spectrum of solid **4**.

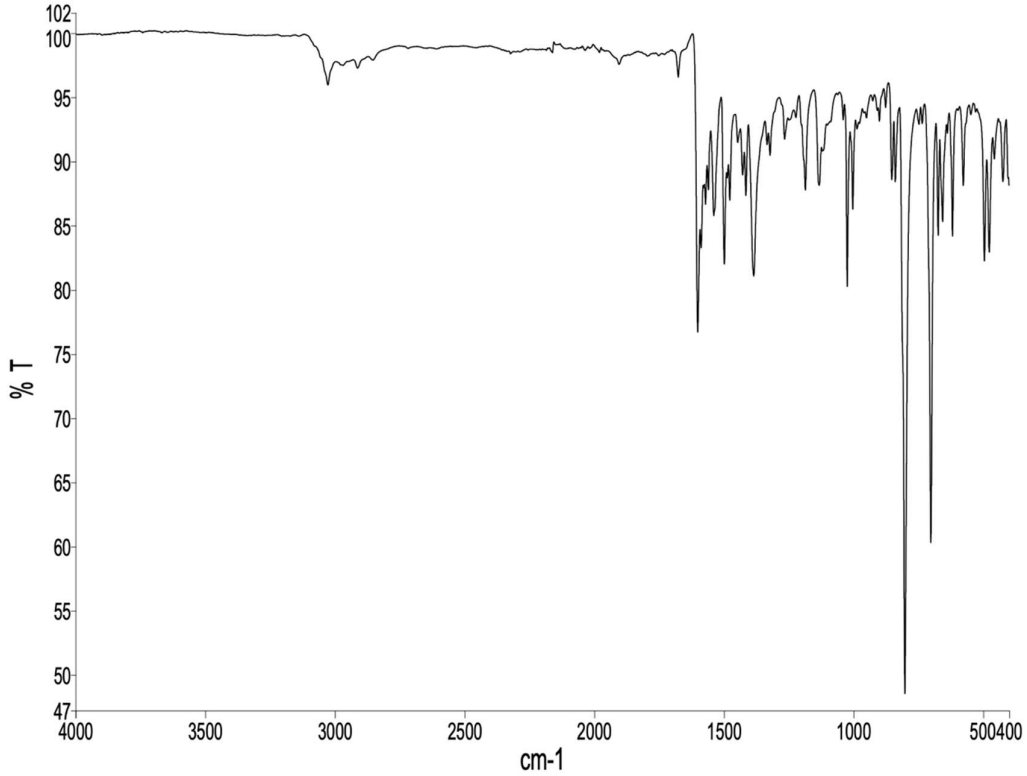

Figure S30. FT-IR spectrum of solid **5**.

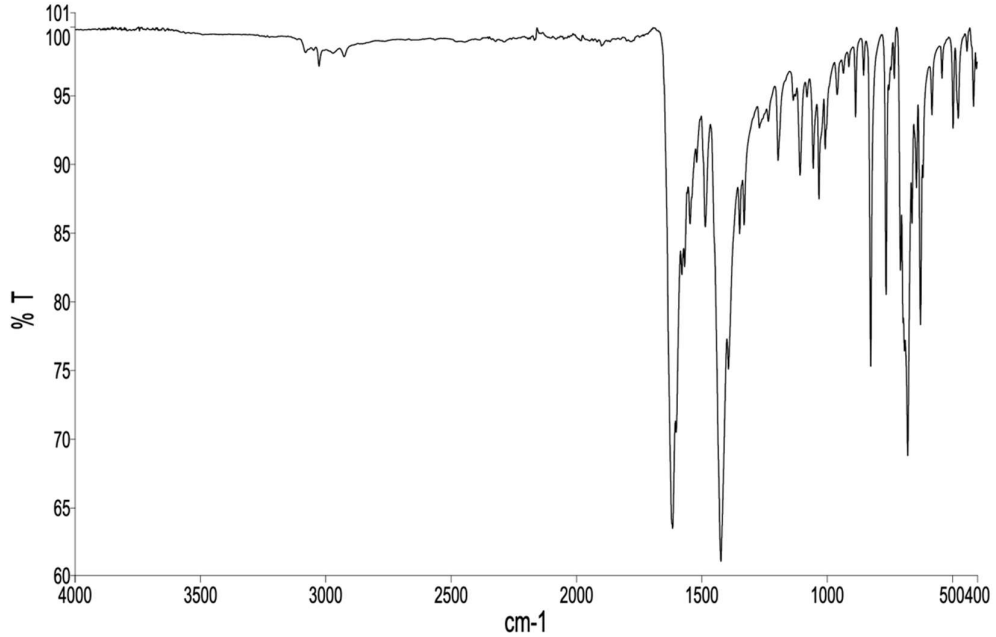

Figure S31. FT-IR spectrum of solid $[Cu_2(\mu\text{-}OAc)_4(\mathbf{1})]_n$.

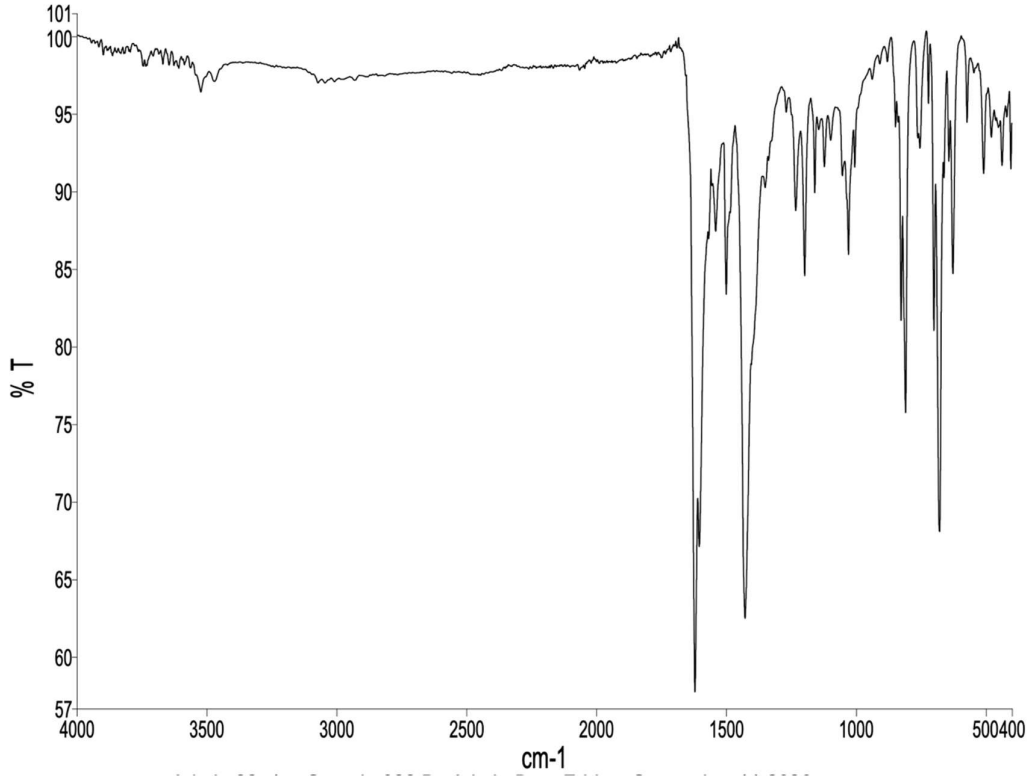

Figure S32. FT-IR spectrum of solid $[Cu_2(\mu\text{-}OAc)_4(\mathbf{2})]_n$.

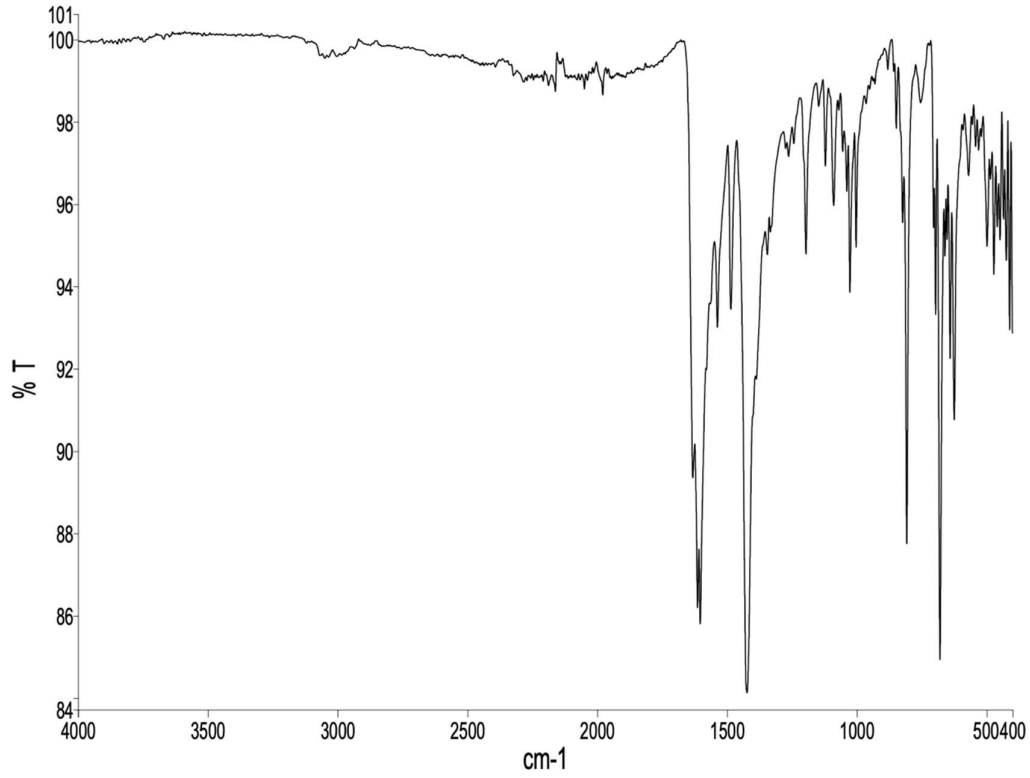

Figure S33. FT-IR spectrum of solid $[Cu_2(\mu\text{-}OAc)_4(\mathbf{3})]_n$.

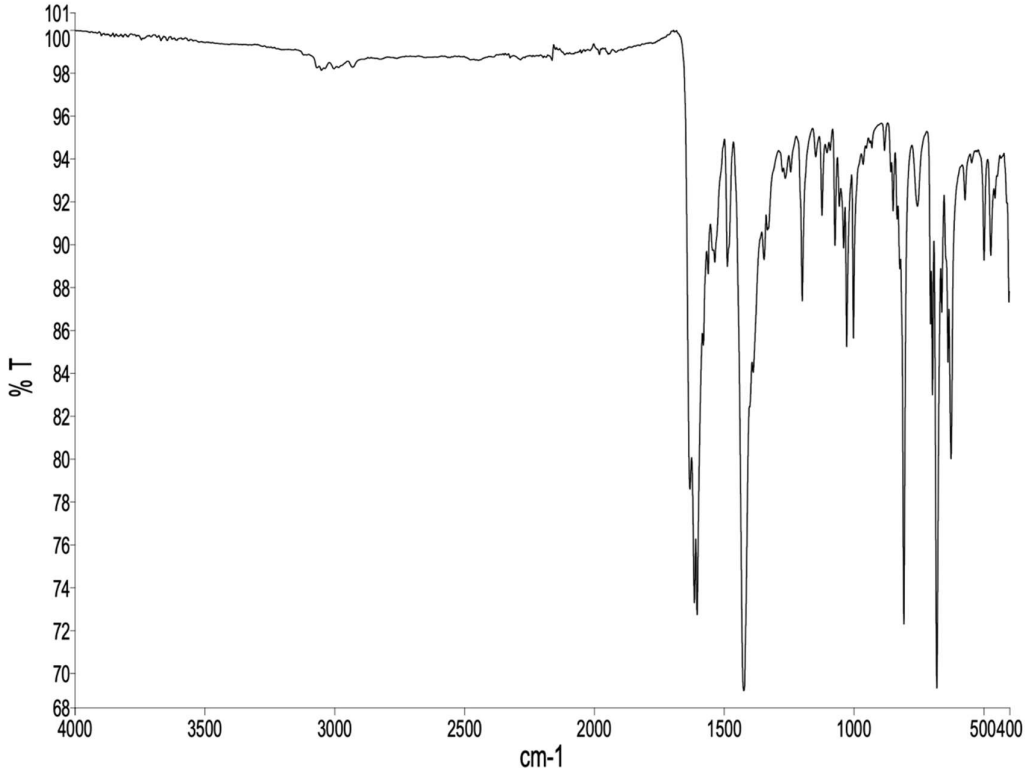

Figure S34. FT-IR spectrum of solid $[Cu_2(\mu\text{-}OAc)_4(\mathbf{4})]_n$.

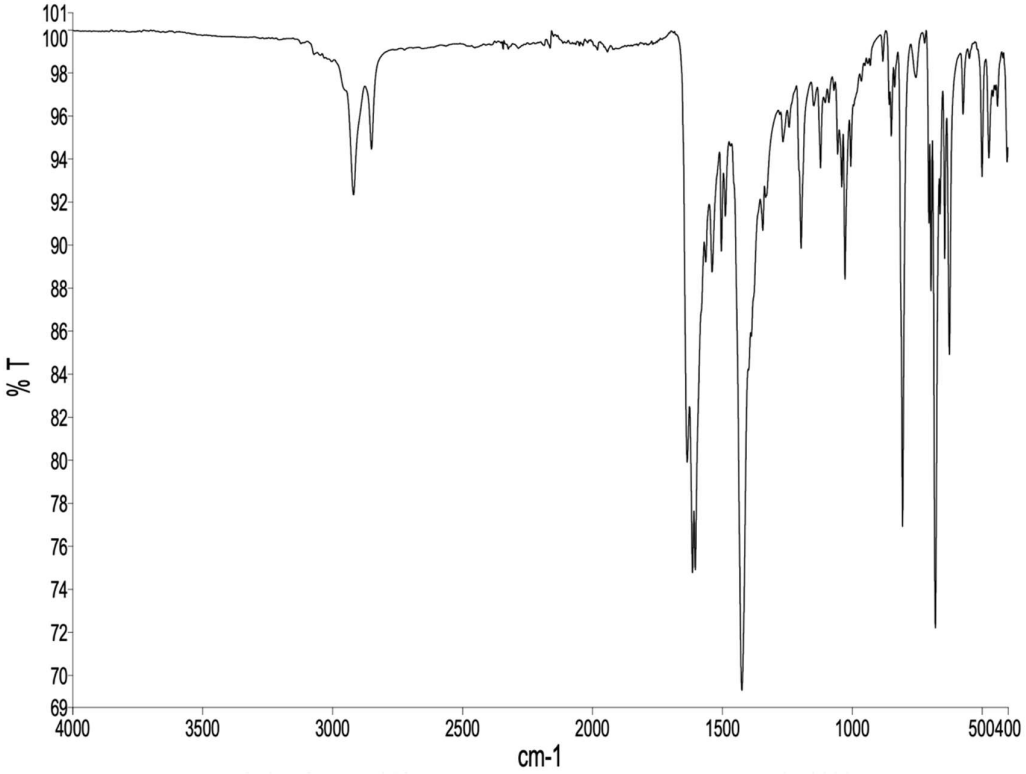

Figure S35. FT-IR spectrum of solid $[Cu_2(\mu\text{-}OAc)_4(\mathbf{5})]_n{\cdot}n$MeOH.

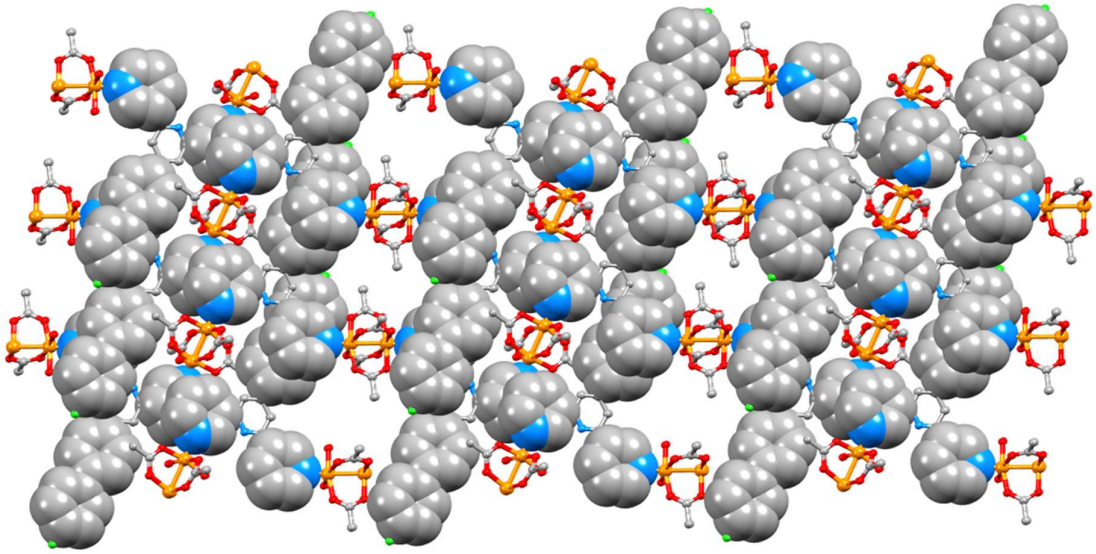

Figure S36. Packing of 1D-coordination polymers in $[Cu_2(\mu\text{-}OAc)_4(\mathbf{3})]_n$.

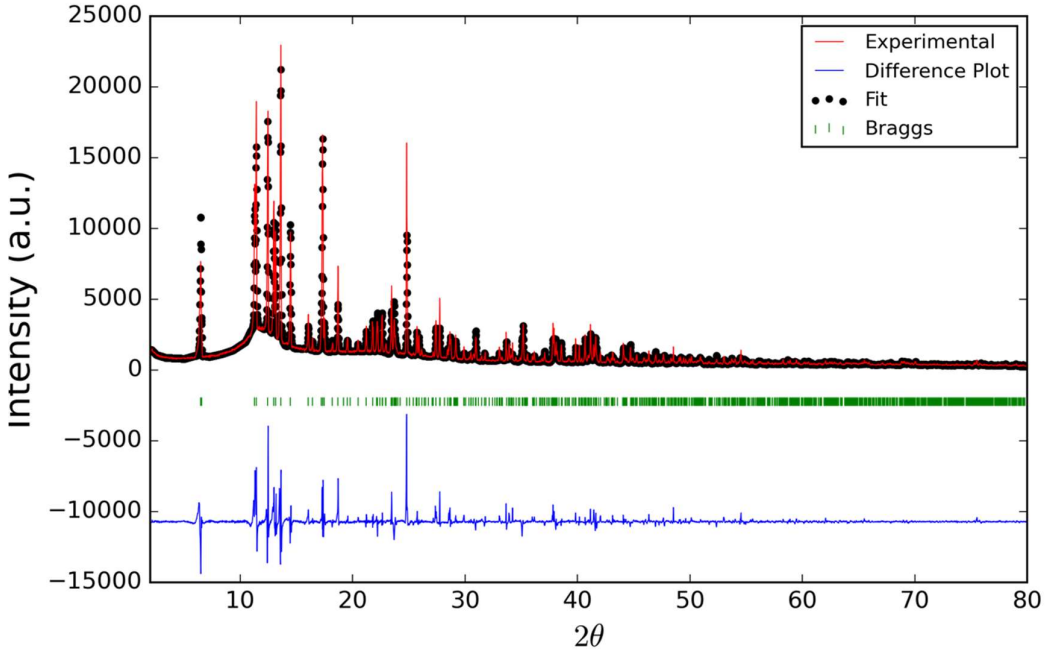

Figure S37. X-Ray diffraction (CuKα1 radiation) pattern (red lines) of the bulk crystalline material of $[Cu_2(\mu\text{-}OAc)_4(\mathbf{1})]_n$ with fitting to the predicted pattern from the single crystal determination. The black dots correspond to the best fits from the Rietveld refinements. Green vertical marks show the Bragg peak positions. The blue line in each plot shows the difference between experimental and calculated points.

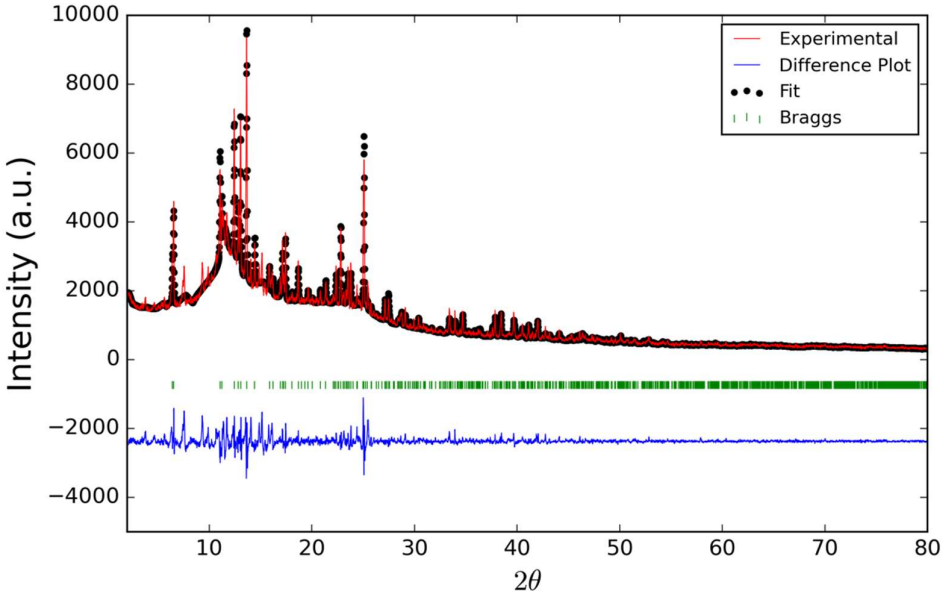

Figure S38. X-Ray diffraction (CuKα1 radiation) pattern (red lines) of the bulk crystalline material of $[Cu_2(\mu\text{-}OAc)_4(\mathbf{2})]_n$ with fitting to the predicted pattern from the single crystal determination. The black dots correspond to the best fits from the Rietveld refinements. Green vertical marks show the Bragg peak positions. The blue line in each plot shows the difference between experimental and calculated points.

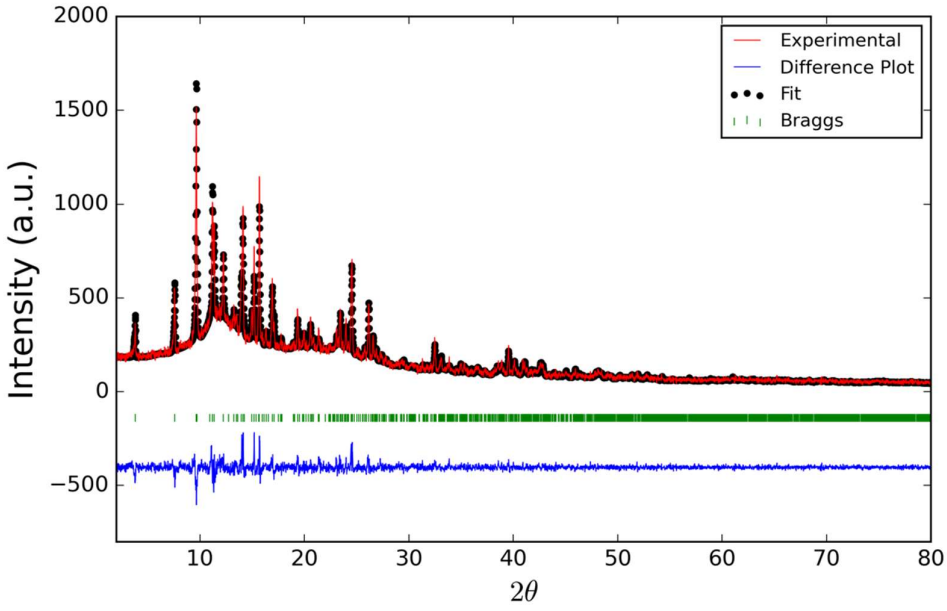

Figure S39. X-Ray diffraction (CuKα1 radiation) pattern (red lines) of the bulk crystalline material of $[Cu_2(\mu\text{-}OAc)_4(\mathbf{3})]_n$ with fitting to the predicted pattern from the single crystal determination. The black dots correspond to the best fits from the Rietveld refinements. Green vertical marks show the Bragg peak positions. The blue line in each plot shows the difference between experimental and calculated points.

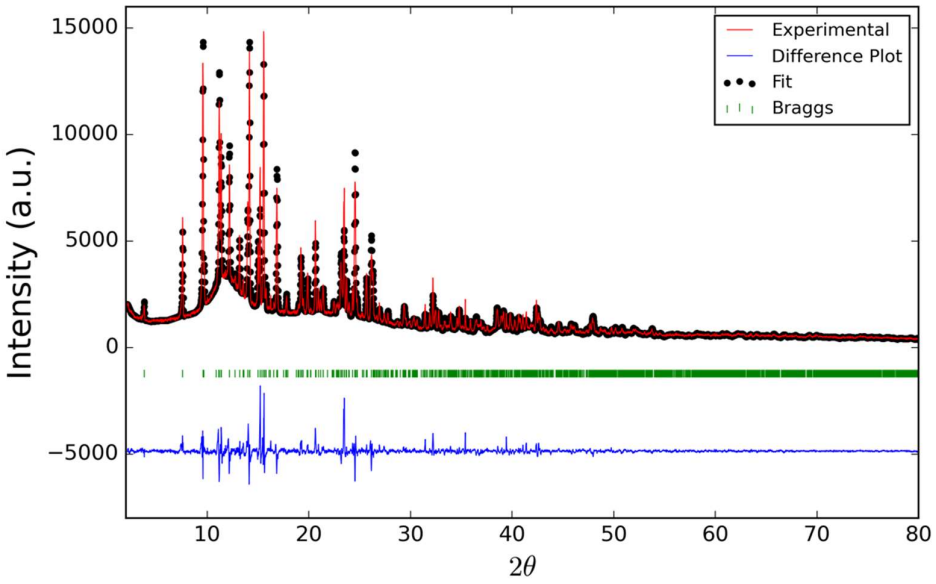

Figure S40. X-Ray diffraction (CuKα1 radiation) pattern (red lines) of the bulk crystalline material of $[Cu_2(\mu\text{-}OAc)_4(\mathbf{4})]_n$ with fitting to the predicted pattern from the single crystal determination. The black dots correspond to the best fits from the Rietveld refinements. Green vertical marks show the Bragg peak positions. The blue line in each plot shows the difference between experimental and calculated points.

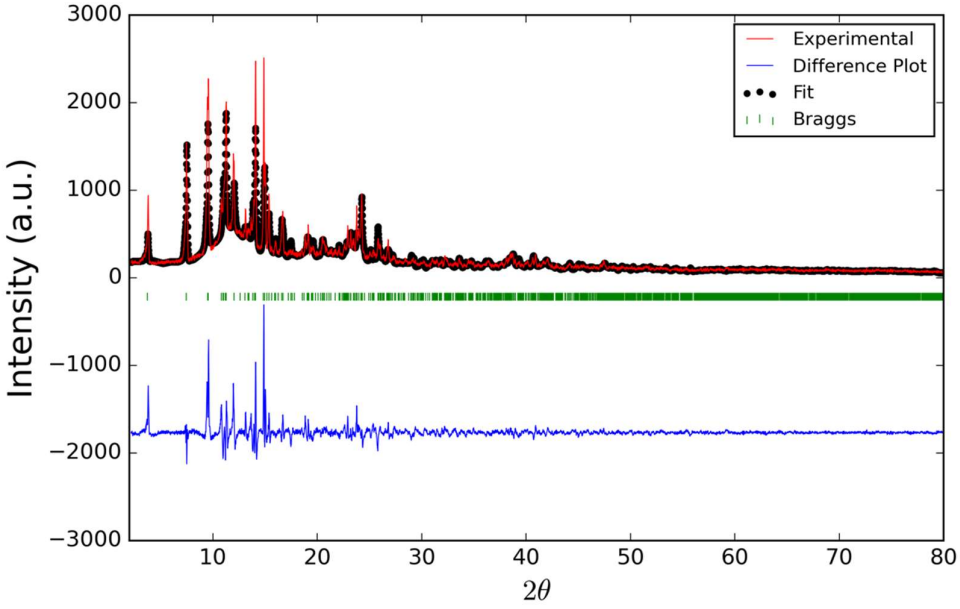

Figure S41. X-Ray diffraction (CuKα1 radiation) pattern (red lines) of the bulk crystalline material of $[Cu_2(\mu\text{-}OAc)_4(\mathbf{5})]_n{\cdot}n$MeOH with fitting to the predicted pattern from the single crystal determination. The black dots correspond to the best fits from the Rietveld refinements. Green vertical marks show the Bragg peak positions. The blue line in each plot shows the difference between experimental and calculated points.

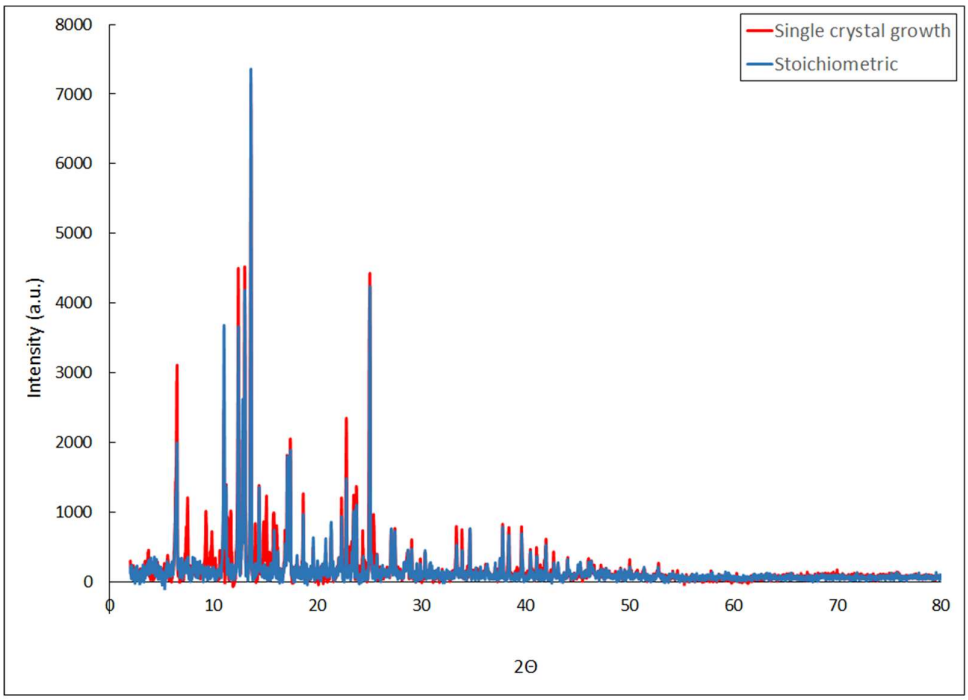

Figure S42. Superimposition of the PXRD patterns of the bulk single-crystalline material of $[Cu_2(\mu\text{-}OAc)_4(\mathbf{2})]_n$ (red line) and of the material from the preparative scale reaction (blue line). The red lines with no match in the blue pattern arise from an impurity in the bulk material from single-crystal growth (see text).

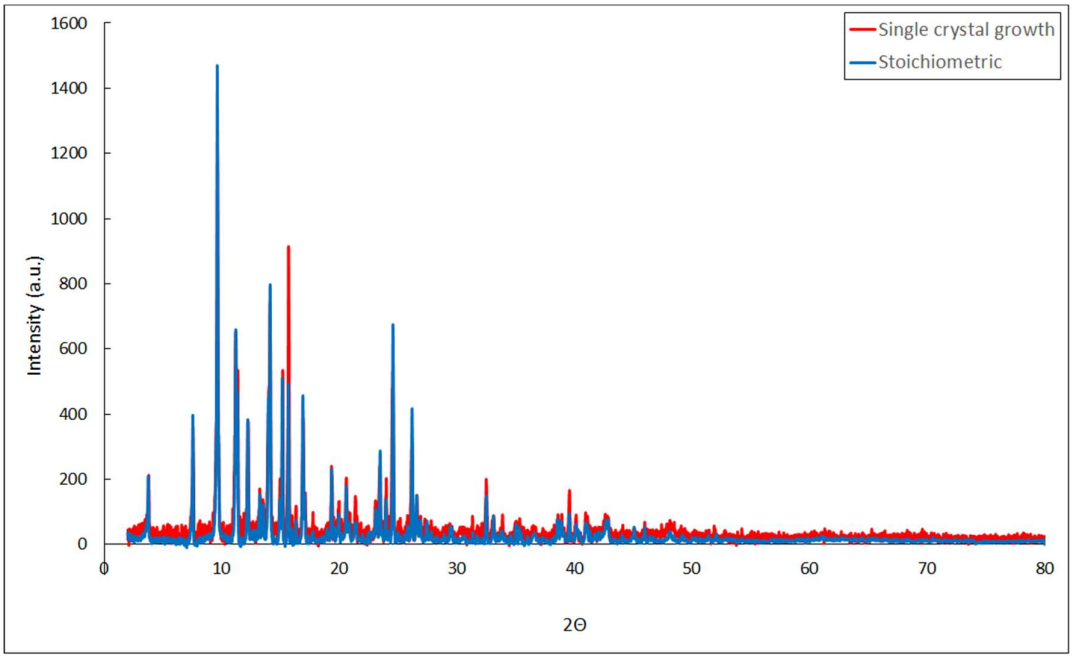

Figure S43. Superimposition of the PXRD patterns of the bulk single-crystalline material of $[Cu_2(\mu\text{-}OAc)_4(\mathbf{3})]_n$ (red line) and of the material from the preparative scale reaction (blue line).

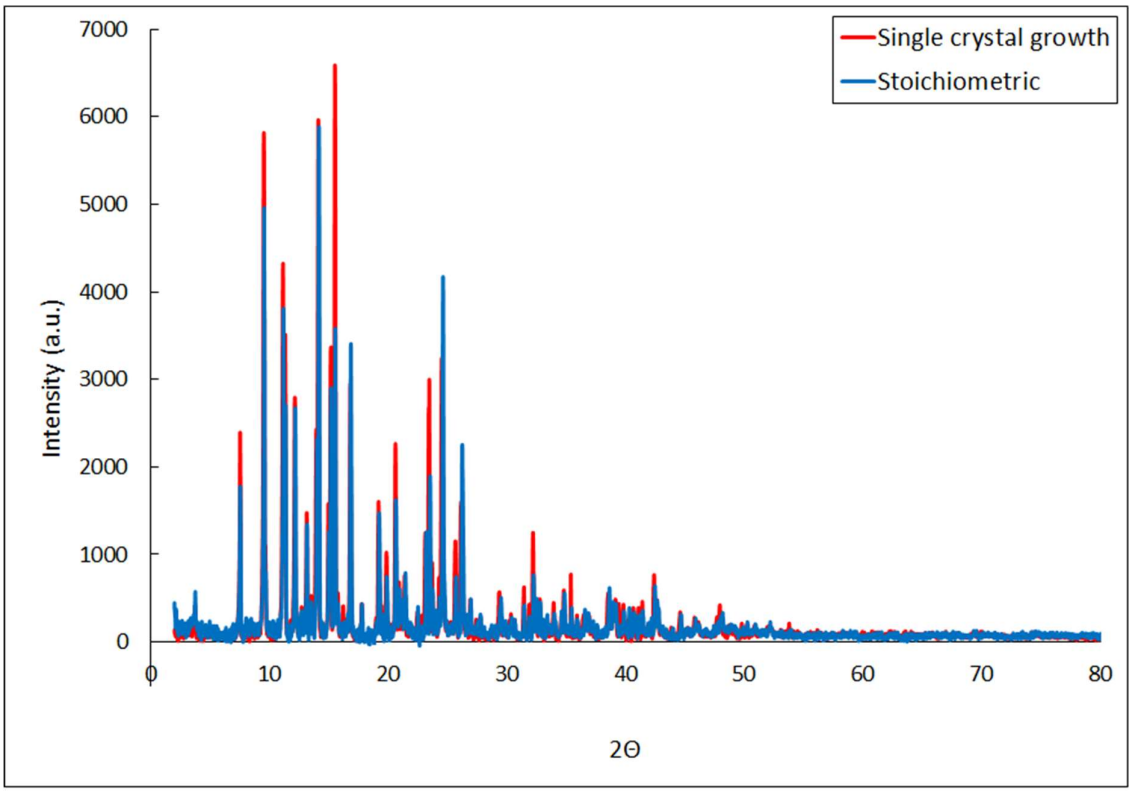

Figure S44. Superimposition of the PXRD patterns of the bulk single-crystalline material of $[Cu_2(\mu\text{-}OAc)_4(\mathbf{4})]_n$ (red line) and of the material from the preparative scale reaction (blue line).

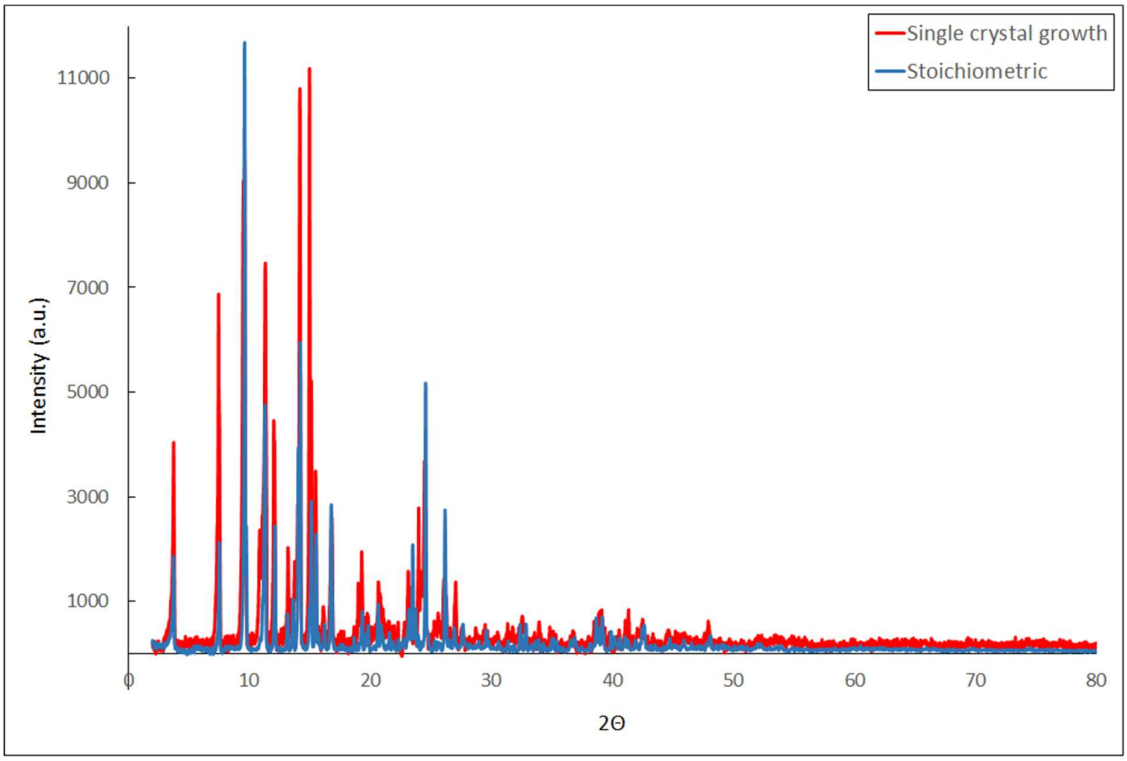

Figure S45. Superimposition of the PXRD patterns of the bulk single-crystalline material of $[Cu_2(\mu\text{-}OAc)_4(\mathbf{5})]_n$ (red line) and of the material from the preparative scale reaction (blue line).